Fission barriers of superheavy nuclei for emitted fragment isotopes near proton magic numbers

R. A. Gherghescu [*] and D. N. Poenaru
Department for Theoretical Physics, Horia Hulubei National Institute for Physics and Nuclear Engineering, Bucharest-Magurele 077125, Romania

(Received 12 August 2022; revised 31 August 2022; accepted 13 September 2022; published 30 September 2022)

Fission barriers for supposed doubly magic ^{298}Fl are calculated using a specialized binary macroscopic-microscopic method. The microscopic effects are obtained from the developed binary Strutinsky shell correction method. The main input data are the proton and neutron energy levels calculated with the deformed two-center shell model. One is able in this way to provide the microscopic transition via the level schemes, from the parent to two overlapped and finally separated level schemes. The macroscopic part is acquired by the deformed charged liquid drop model with the double Yukawa-plus-exponential finite range potential. The method is applied to the reactions accompanied by isotopes of Sn and Pb within the fission channels, as being favored by strongly negative shell corrections.

DOI: 10.1103/PhysRevC.106.034616

I. INTRODUCTION

Superheavy nuclei survive only due to shell effects. The macroscopic part of the fission barrier is close to zero for most of the possible decay channels. Due to negative shell effects, a pocket in the total deformation energy is formed, capable to accommodate the quasistable ground state of the parent. Along the decay process, various barrier shapes are generated, depending on the nucleus deformation. For example, the height of the static spontaneous fission barrier for superheavy nuclei is calculated with the macroscopic-microscopic method [1]. Axial symmetry of the parent nucleus is assumed for $Z = 98$–102 in [1]. The deformation space used is β_λ=2, 4, 6, 8. The crucial shell corrections are obtained by the Strutinsky method for one level scheme of the Woods-Saxon potential, so the barrier is the result of the parent nucleus deformation in the $\{\beta_\lambda\}$ space.

Fission barriers for superheavy nuclei are approximated in [2,3] using the Q_α values of the measured decay chains. The data are compared with the predictions of macroscopic-microscopic models. Thus, fission barriers are estimated as being a major factor contributing to the total cross section. However, the Q values give information only on the separated fragment configuration.

The deformed nuclear shapes are obtained in [4] by an expansion in Legendre polynomials and perturbed spheroids. Shell corrections are computed with the Woods-Saxon (one center again) and modified oscillator potential.

The potential barriers have been studied within the generalized liquid drop model, taking into account the proximity forces acting between surfaces in regard to the charge and mass asymmetry and the shell effects [5]. Transition is made from one to two spheres. In very asymmetric channels, one-hump potential barriers appear. Reference [5] is related to the present paper, as it takes into account various decay reaction channels.

Fission probabilities are calculated using the "fusion by diffusion" model [6]. Here the ground state, saddle point properties and masses, shell corrections, and deformation are calculated systematically within the multidimensional macroscopic-microscopic method, based on the deformed Woods-Saxon single-particle potential.

Stability and fission barrier height, being assimilated as shell effects, are experimentally studied for ^{254}No and ^{220}Th [7]. The extracted barrier agrees with the values predicted by the macroscopic-microscopic model. Discrepancies are underlying the single-particle spectra differences, hence the domination of the shell energy.

The spontaneous fission process is studied within a semiempirical WKB approximation [8]. The potential barrier is obtained using the generalized liquid drop model, taking into account the nuclear proximity and mass asymmetry. The shape-dependent shell corrections have been determined within the droplet model, which gets the energy levels from an axially deformed Woods-Saxon potential and applying the Strutinsky method. The model is again a one center equivalent.

Potential energy surfaces of superheavy nuclei are evaluated again within the single macroscopic-microscopic approximation [9]. A liquid drop type of mass formula is used to determine the macroscopic part of the nuclear energy, and the Strutinsky method is used again for shell corrections. A mean-field potential is used to obtain the energy levels as eigenvalues of the corresponding Hamiltonian. Nuclear shapes are obtained through a Fourier shape parametrization, starting from the expansion of a sphere, followed by deformation.

The fission barriers of compound nuclei are studied with the time-dependent Hartree-Fock + BCS (TD-BCS) approach

[*] radu@theory.nipne.ro

[10]. The initial configuration of the compound nucleus is obtained by finite-temperature TD-BCS calculations. Fission pathways forming the barrier in the quadrupole-octupole deformation space are obtained mainly for two asymmetric channels, at A_H=135.0 and 138.7. Self-consistent calculation using the Skyrme force is applied to obtain the fission energy curve of ^{240}Pu. [11]. Double-humped barriers are visible for the actinide region, as expected. No information about a specific fission channel can result here. A two-dimensional, self-consistent Thomas-Fermi calculation of fission barriers, adapted to rotating nuclei at finite temperature, is described in [12]. It is shown that the computed fission barrier decreases with increasing temperature and angular momentum. Fission barriers of ^{254,256,258}Fm, ^{258}No, and ^{260}Rf are investigated in a fully microscopic way up to the scission point [13]. The analysis is based on the constrained Hartree-Fock-Bogoliubov theory and Gogny D1S force. The quadrupole, octupole, and hexadecapole moments as well as the number of nucleons in the neck region are used as constraints. Two fission paths are found. Sn influence is emphasized in the two proton-symmetric fission channel from ^{256}Fm for the barrier obtained along the quadrupole (elongation) coordinate. The systematics of fission barriers in superheavy elements, in the range $Z = 108$–120 and $N = 166$–182, are investigated with the relativistic mean field (RMF) model, as well as with the nonrelativistic Skyrme-Hartree-Fock approach [14]. As a comparison, the RMF predicts lower barriers than most Skyrme interactions. As related to the present paper, heights of the fission barriers are obtained as a function of the neutron numbers. The barriers for the superheavy Fl are close to the ones calculated in this paper for special fission channels. Static fission barriers of even-even nuclei with $100 \leqslant Z \leqslant 110$ are investigated using again the Skyrme-Hartree-Fock model [15]. The energy density functional defined by the Skyrme SLy4 and the seniority pairing force are used. Static fission paths defining the barriers are obtained as reflection symmetric for ^{264}Fm due to doubly magic fragment ^{132}Sn. The dependence of fission barriers on the excitation energy of the compound nucleus upon the survival probability of superheavy nuclei is also studied with the self-consistent nuclear density functional theory [16]. One predicts a rapid decrease of the barrier with temperature for ^{278}Cn as compared to ^{292}Fl, but again, no fission channel can be mentioned.

The barrier is taken as the Coulomb and proximity potential sum in [17]. Different expressions for the universal proximity potential function are given for different stages of the binary configuration. The barrier height is calculated here for every possible heavy-light nucleus channel. Spherical shapes are considered and shell effects are taken phenomenologically. Also, using the same model, the shell effects are accounted for via the Q values [18] and the fission path barrier is taken as the minimum driving potential with respect to the mass and charge asymmetries. These calculations are related to the present paper. They confirm the role of doubly magic or nearly doubly magic configurations in fission. They also stress that, in addition to closed shell effect, ground state deformation also plays an important role in determining the isotopic yield in the fission process. Of course, shell effects decrease with the excitation energy of the system [19].

The Q values contain the shell effects for the final stage of the decay process, and consequently influence the fission barrier [20]. This quantity has been calculated using the isospin cluster model and α-decay half-lives could be obtained. It proves the impact of magicity, here namely the supposed neutron closure at N=172.

The quantum mechanical fragmentation theory and the preformed cluster-decay model are used to get the α-decay half-lives [21]. Using the Strutinsky method, one shows that motions in η and η_Z asymmetries are faster that the R motion (elongation). It is also mentioned that the attraction between nuclear surfaces changes the relative heights of the potential energy minima (i.e., fission barrier height). Another related approach uses α-nucleus interaction potentials with M3Y deformation energy, forming the barrier which comprises the sum of the nuclear, Coulomb, and centrifugal energies [22,23]. The fragmentation theory is extended for the generalized nuclear proximity potential where the deformations are included [24]. The fragmentation potential generates the fission barrier by including the binding energy, Coulomb, and nuclear proximity terms. The calculations are made also for nonoverlapping nuclei.

The importance of mass asymmetry coordinates is stressed along with the relative separation among the decay fragments, for the estimation of the penetration barrier. The impact of the fragmentation potential on the interaction, and therefore on the barrier, is studied for different fission channel fragment combinations in [25]. Reference [25] is more related to the present paper. The importance of the transition region where the two fragments are partially overlapped is stressed within the model we are using. We present a theoretical approach being able to account for a specific spontaneous fission channel. The charge and mass asymmetry are given from the beginning, and the influence of the partially overlapped level schemes is underlined with respect to the shell corrections, and consequently on the fission barriers.

Section II presents the theoretical basis of the model, a very specialized binary macroscopic-microscopic method for fission. In Sec. III the resulting fission barriers are displayed and discussed, followed by Conclusions.

II. THEORETICAL BINARY METHOD

The most appropriate fissionlike configuration is described by two intersected spheroids forming an axially symmetric shape. The corresponding barrier is constructed in two main parts: the macroscopic term $E_{\rm mac}$, where the only deformation dependent energies are the Coulomb and the finite range nuclear ones, and the microscopic term $E_{\rm shell}$, played by the shell corrections. The last one is totally dependent on the transition of the parent proton and neutron level schemes from a singular potential well to two overlapped and then separated ones. These level schemes are input data for the Strutinsky method. The two terms which form the fission barrier E_b, when applied to the appropriate shape evolution, should describe the binary process energetically:

$$E_b = E_{\rm mac} + E_{\rm shell}. \tag{1}$$

Each one is presented in the following subsections.

A. The macroscopic Yukawa-plus-exponential energy

A charged liquid drop with finite range nuclear forces acting on the surface generates the binary macroscopic term. It follows the splitting transition from the parent shape, through the two partially overlapped spheroids (heavy-daughter and light-emitted fragment) up to separated nuclei. The total deformation dependent macroscopic energy reads

$$E_{\rm mac} = \left(E_C - E_C^{(0)}\right) + \left(E_{\rm YE} - E_{\rm YE}^{(0)}\right) \tag{2}$$

where E_C and $E_{\rm YE}$ are the Coulomb and finite range Yukawa-plus-exponential (YE) energies. $E_C^{(0)}$ and $E_{\rm YE}^{(0)}$ are the energies for the initial parent nucleus values. The balance between these two forces generates the macroscopic barrier. These two terms vary with deformation in the charged liquid drop energy.

The Coulomb term is calculated as [26]

$$E_C = \frac{2\pi}{3}\left(\rho_{eH}^2 F_{CH} + \rho_{eL}^2 F_{CL} + 2\rho_{eH}\rho_{eL}F_{CHL}\right) \tag{3}$$

where ρ_{eH} and ρ_{eL} are the charge densities of the heavy and light fragments. The last term accounts for the Coulomb interaction between the reaction partners. F_{CH}, F_{CL}, and F_{CHL} are only shape dependent integrals:

$$\begin{aligned} F_{CH} &= \int_{-a_1}^{z_s} dz \int_{-a_1}^{z_s} dz' G_H(z,z'), \\ F_{CL} &= \int_{z_s}^{R+a_2} dz \int_{z_s}^{R+a_2} dz' G_L(z,z'), \\ F_{CHL} &= \int_{-a_1}^{z_s} dz \int_{z_s}^{R+a_2} dz' G_{HL}(z,z') \end{aligned} \tag{4}$$

where a_1 and a_2 are the spheroid semiaxes along the symmetry axis, z_s is the separation point, and R is the distance between the fragment centers. The Coulomb integrands read

$$\begin{aligned} G_i(z,z') = &\left\{\rho_i(z)\rho_i(z')\frac{K(k)-2D(k)}{3}\left[2\left(\rho_i^2(z)+\rho_i^2(z')\right) - (z-z')^2 + 1.5(z-z')\left(\frac{d\rho_i^2(z')}{dz'} - \frac{d\rho_i^2(z)}{dz}\right)\right]\right. \\ &\left. + K(k)\left\{\frac{\rho_i^2(z)\rho_i^2(z')}{3} + \left[\rho_i^2(z) - 0.5(z-z')\frac{d\rho_i^2(z)}{dz}\right]\left[\rho_i^2(z') + 0.5(z-z')\frac{d\rho_i^2(z')}{dz'}\right]\right\}\right\} \\ &\times \frac{1}{[(\rho_i(z)+\rho_i(z'))^2 + (z-z')^2]^{1/2}} \end{aligned} \tag{5}$$

where i stands for H and L individual fragment terms. $\rho_{H,L}(z)$ are the nuclear surface equations in cylindrical coordinates, for axially symmetric shapes. The third Coulomb integrand responsible for the H-L interaction reads

$$\begin{aligned} G_{HL}(z,z') = &\left\{\rho_H(z)\rho_L(z')\frac{K(k_{HL})-2D(k_{HL})}{3}\left[2\left(\rho_H^2(z)+\rho_L^2(z')\right) - (z-z')^2 + 1.5(z-z')\left(\frac{d\rho_H^2(z')}{dz'} - \frac{d\rho_L^2(z)}{dz}\right)\right]\right. \\ &\left. + K(k_{HL})\left\{\frac{\rho_H^2(z)\rho_L^2(z')}{3} + \left[\rho_H^2(z) - 0.5(z-z')\frac{d\rho_H^2(z)}{dz}\right]\left[\rho_L^2(z') + 0.5(z-z')\frac{d\rho_L^2(z')}{dz'}\right]\right\}\right\} \\ &\times \frac{1}{[(\rho_H(z)+\rho_L(z'))^2 + (z-z')^2]^{1/2}}. \end{aligned} \tag{6}$$

The spherical Coulomb term is

$$E_{C_0} = \frac{3Z^2e^2}{5r_0A^{1/3}}. \tag{7}$$

The second component of the macroscopic energy is generated by the finite range nuclear surface forces and produces the YE energy [27], which reads

$$E_{\rm YE} = \frac{1}{4\pi r_0^2}\left[c_{sH}D_{Y_H} + c_{sL}D_{Y_L} + 2(c_{s_H}c_{s_L})^{1/2}D_{Y_{HL}}\right] \tag{8}$$

where [26]

$$D_{Y_H} = \int_0^{2\pi}\int_{-a_1}^{z_s}\int_{-a_1}^{z_s} E_{Y_H}^{(1)}E_{Y_L}^{(1)}Q^{(1)}d\phi dz dz', \tag{9}$$

$$D_{Y_L} = \int_0^{2\pi}\int_{z_s}^{R+a_2}\int_{z_s}^{R+a_2} E_{Y_H}^{(2)}E_{Y_L}^{(2)}Q^{(2)}d\phi dz dz', \tag{10}$$

$$D_{Y_{HL}} = \int_0^{2\pi}\int_{-a_1}^{z_s}\int_{z_s}^{R+a_2} E_{Y_H}^{(12)}E_{Y_L}^{(12)}Q^{(12)}d\phi dz dz'. \tag{11}$$

(12)

The integrand terms are

$$\begin{aligned} E_{Y_H}^{(i)} &= \rho_i^2(z) - \rho_i(z)\rho_i(z')\cos\phi - 0.5(z-z')\frac{d\rho_i^2(z)}{dz}, \\ E_{Y_L}^{(i)} &= \rho_i^2(z') - \rho_i(z)\rho_i(z')\cos\phi + 0.5(z-z')\frac{d\rho_i^2(z')}{dz'}, \\ Q^{(i)} &= 2 - \left[\left(\frac{\sigma_i}{a}\right)^2 + 2\frac{\sigma_i}{a} - 2\right]e^{-\frac{\sigma_i}{a}}\frac{1}{\sigma_i^4} \end{aligned} \tag{13}$$

with $i = H, L$, and

$$\sigma_i = \left[\rho_i^2(z) + \rho_i^2(z') - 2\rho_i(z)\rho_i(z')\cos\phi + (z-z')^2\right]^{1/2}. \tag{14}$$

The interaction term for the Yukawa energy reads

$$E_{Y_H}^{(HL)} = \rho_H^2(z) - \rho_H(z)\rho_L(z')\cos\phi - 0.5(z-z')\frac{d\rho_H^2(z)}{dz},$$

$$E_{Y_L}^{(HL)} = \rho_L^2(z') - \rho_H(z)\rho_L(z')\cos\phi + 0.5(z-z')\frac{d\rho_L^2(z')}{dz'},$$

$$Q^{(HL)} = 2 - \left[\left(\frac{\sigma_{HL}}{a}\right)^2 + 2\frac{\sigma_{HL}}{a} - 2\right]e^{-\frac{\sigma_{HL}}{a}}\frac{1}{\sigma_{HL}^4}, \tag{15}$$

and

$$\sigma_{HL} = \left[\rho_H^2(z) + \rho_L^2(z') - 2\rho_H(z)\rho_L(z')\cos\phi + (z-z')^2\right]^{1/2}. \tag{16}$$

The spherical Yukawa-plus-exponential part is

$$E_Y^{(0)} = \left\{1 - 3\left(\frac{a}{R_0}\right)^2 + \left(\frac{R_0}{a} + 1\right)\left[2 + 3\frac{a}{R_0} + 3\left(\frac{a}{R_0}\right)^2\right]e^{-\frac{2R_0}{a}}\right\}E_S^{(0)} \tag{17}$$

where

$$E_S^{(0)} = c_s A^{2/3}. \tag{18}$$

The intermediate surface coefficients read

$$c_{s_i} = a_s\left[1 - \kappa\frac{N_i - Z_i}{A_i}\right]. \tag{19}$$

The use of these expressions ensures taking into account the Coulomb and nuclear surface interaction between the two partially splitting fragments within the macroscopic deformation energy.

B. Shell effects

The shell effects are the reason superheavy nuclei exist. The shell correction term allows the survival of such a massive system, overcoming the large electrostatic repulsion. When a negative value occurs, a pocket in the total deformation energy is generated. Thus, the energy minimum so formed accommodates the ground state of the parent nucleus. At the same time, a potential barrier rises against any possible fission channel. In order to calculate the values of the shell corrections, one has to keep in mind the following.

(1) The input data for computing these microscopic energies must be the proton and neutron level schemes.

(2) The proton and neutron level schemes must follow the geometry of the fission configuration.

(3) Such a requirement is acquired by a specialized potential able to follow the microscopic transition from one quantum well, the parent one, through two partially overlapped configurations, up to two separated wells, each one corresponding to the correct level scheme of the individual fission fragments. Such a specialized shell model shall be briefly presented, followed by the binary shell correction procedure.

1. The deformed two-center shell model

A specialized microscopic tool to assess for the changes within the structure of the binary configuration is provided by the two-center shell model. The symmetric version was presented for the first time in [28] and used in two-molecular state studies. An asymmetric spherical two-center shell model has been developed for nuclei in [29], based on two spherical oscillators. Another version takes advantage of the more realistic finite wells of two Woods-Saxon based potentials to achieve the binary configuration structure [30]. All the above demands are also fulfilled by the deformed two-center shell model (DTCSM) [31]. The model is based on two deformed, partially overlapped, oscillators, as the core of the potential:

$$V_{\rm DTCSM}(\rho,z) = \begin{cases} V_H(\rho,z) = \frac{1}{2}m_0\omega_{\rho_H}^2\rho^2 + \frac{1}{2}m_0\omega_{z_H}^2(z+z_H)^2, & \text{for } A_H \\ V_L(\rho,z) = \frac{1}{2}m_0\omega_{\rho_L}^2\rho^2 + \frac{1}{2}m_0\omega_{z_L}^2(z-z_L)^2, & \text{for } A_L \end{cases} \tag{20}$$

where z_H and z_L are the centers of the heavy and light fragments. The frequencies ω_{ρ_i} and ω_{z_i} are shape dependent, being related to the spheroids semiaxes of each of the fragments. The residual interactions of spin-orbit $\hat{l}\hat{s}$ and the squared orbital momentum $\hat{l}^2$ are added:

$$V_{\hat{l}\hat{s}} = \begin{cases} -\left\{\frac{\hbar}{m_0\omega_{0H}}\kappa_H(\rho,z), (\nabla V_{\rm DTCSM}\times\hat{p})\hat{s}\right\}, & A_H - \text{region} \\ -\left\{\frac{\hbar}{m_0\omega_{0L}}\kappa_L(\rho,z), (\nabla V_{\rm DTCSM}\times\hat{p})\hat{s}\right\}, & A_L - \text{region} \end{cases} \tag{21}$$

and

$$V_{\hat{l}^2} = \begin{cases} -\left\{\frac{\hbar}{m_0^2\omega_{0H}^3}\kappa_H\mu_H(\rho,z), (\nabla V_{\rm DTCSM}\times\hat{p})^2\right\}, & A_H - \text{region} \\ -\left\{\frac{\hbar}{m_0^2\omega_{0L}^3}\kappa_L\mu_L(\rho,z), (\nabla V_{\rm DTCSM}\times\hat{p})^2\right\}, & A_L - \text{region} \end{cases} \tag{22}$$

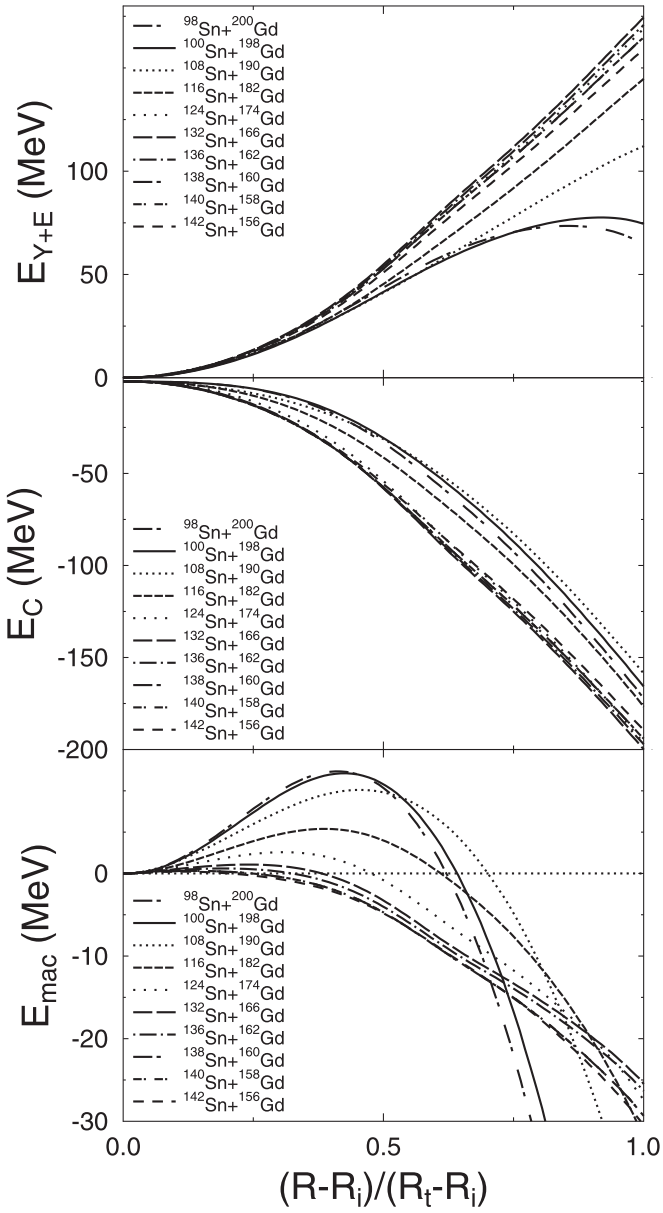

FIG. 1. Comparison of Coulomb, Yukawa-plus-exponential, and macroscopic barrier terms against the reduced distance between centers for Sn fission channels from ^{298}Fl.

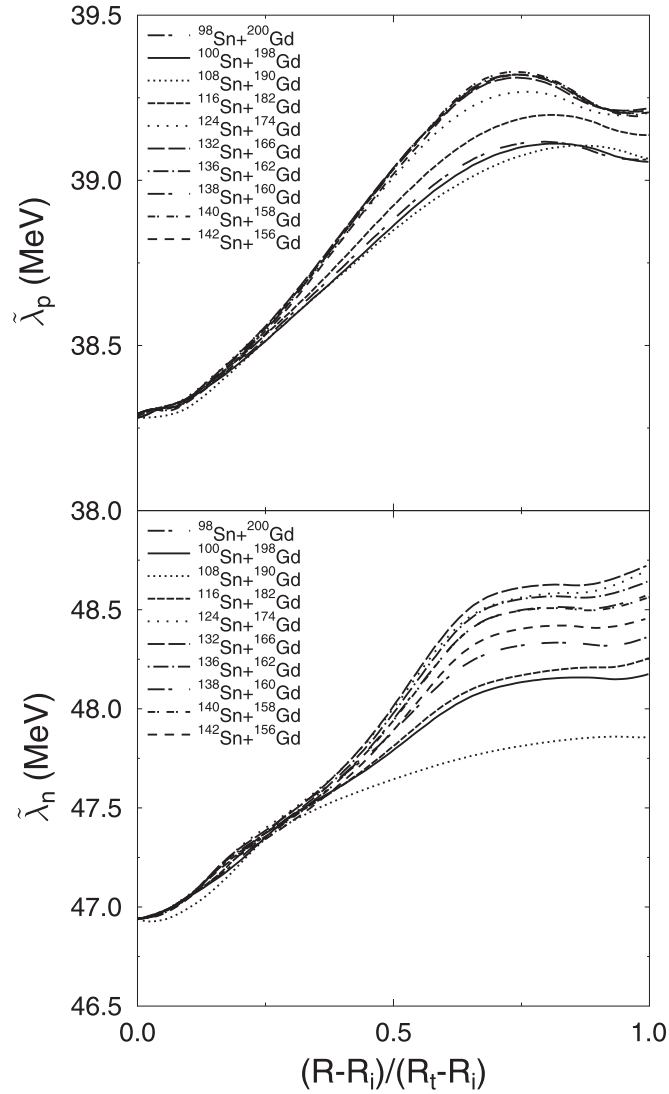

FIG. 2. Comparison between the smoothed distribution Fermi level for protons and neutrons against the reduced distance between centers, for Sn fission channels from ^{298}Fl. The ^{142}Sn reaction has the highest proton and neutron Fermi level during the overlapping configuration.

where $\kappa_{H,L}(\rho, z)$ and $\mu_{H,L}(\rho, z)$ are the usual interaction strength function parameters for the heavy and light fragment regions A_H and A_L. The Schrödinger equation is solved for the total Hamiltonian H_{DTCSM},

$$H_{\text{DTCSM}} = -\frac{\hbar^2}{2m_0}\Delta + V_{\text{DTCSM}}(\rho, z) + V_{\hat{l}\hat{s}}(\rho, z) + V_{\hat{l}^2}(\rho, z), \tag{23}$$

separately for protons and neutrons. As a result, the sequence of level schemes will describe the microscopic transition from the parent to two overlapped and finally separated fragment energy levels.

2. The Strutinsky binary method

The sequence of level schemes enters as input data in the Strutinsky procedure. One notes that the energy levels already carry the binary microscopic character for the fission process. The pairing corrections are missing. One knows that the pairing energy smears out the shell effects. Their energy value has always an opposite sign to the shell ones. Moreover, the absolute value of the pairing energy is about 0.2 of the shell corrections. Due to these assumptions, one states that the pairing interaction changes a little the shape of the barrier, but not much of the height or the width. Thus, one can assume that the ordering of the fission barriers for different channels does not change. Consequently, as a first approximation, at this stage of the calculations the pairing corrections have been neglected, but will be considered in the future.

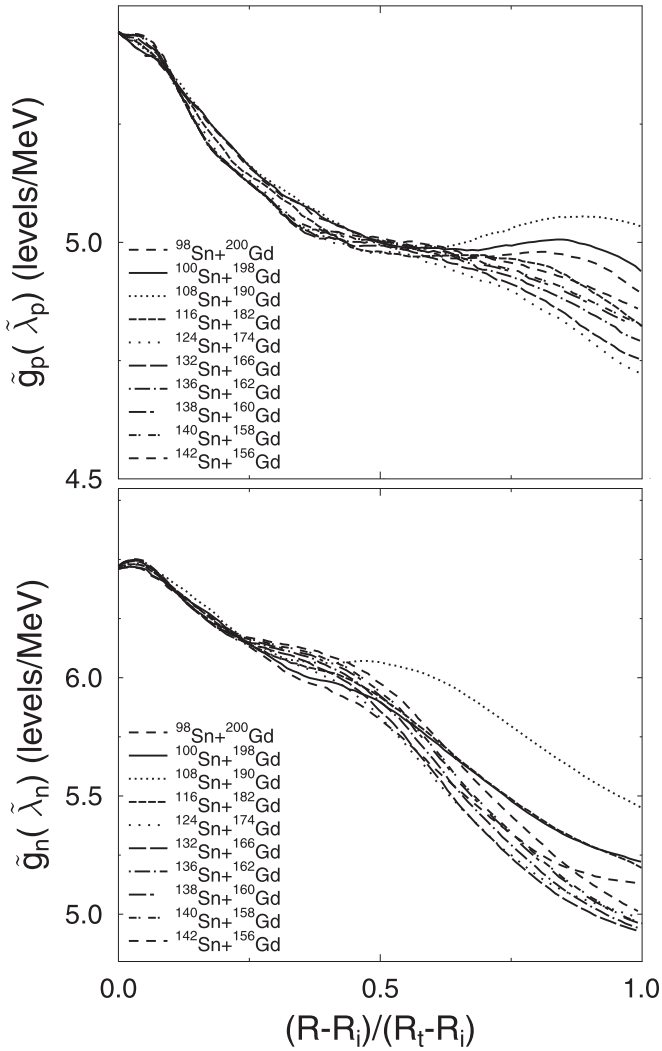

FIG. 3. Comparison between the proton $\tilde{g}_p(\tilde{\lambda}_p)$ and neutron $\tilde{g}_n(\tilde{\lambda}_n)$ smoothed densities evolution at the Fermi level against the reduced distance between centers, for Sn fission channels from ^{298}Fl. The last part of the variation is mainly due to the individual fragment level schemes influence.

At every step of the decay, the shell corrections are calculated separately for protons and neutrons,

$$E_{\mathrm{sh}_{p,n}} = \sum_{\nu=1}^{n} 2E_\nu - \tilde{U}, \tag{24}$$

and the results are added:

$$E_{\mathrm{shell}} = E_{\mathrm{sh}_p} + E_{\mathrm{sh}_n}. \tag{25}$$

$\{E_\nu\}$ are the DTCSM energy levels. The important quantity to be computed is $\tilde{U}$, the "smoothed part" of the spectrum, which is the total level energy if the levels are uniformly distributed. One defines a smoothed-level distribution energy $\tilde{g}(\epsilon)$ by the average of the real one over an arbitrary interval, here $\gamma \approx \hbar\omega_0$:

$$\tilde{g}(\epsilon) = \int_{-\infty}^{\infty} \zeta\left(\frac{\epsilon-\epsilon'}{\gamma}\right) g(\epsilon') = \frac{1}{\gamma}\sum_i \zeta\left(\frac{\epsilon-\epsilon_i}{\gamma}.\right) \tag{26}$$

One uses as a smoothing function

$$\zeta(x) = \frac{1}{\sqrt{\pi}} e^{-x^2} \sum_{k=0}^{m} a_{2k} H_{2k(x)} \tag{27}$$

where $H_k(x)$ are the Hermite functions. This quantity becomes important in calculating the total smoothed energy $\tilde{U}$. As a difference from the usual Strutinsky procedure, one obtains the smoothed density as influenced by both heavy and light fragments, via the DTCSM levels. The smoothing takes place up to the smoothed distribution Fermi level $\tilde{\lambda}$. The $\tilde{\lambda}$ energy will determine how much one subtracts from the initial level sum, and subsequently how deep the shell correction will be within the total energy at every step of the splitting. The smoothed Fermi level is obtained from the conservation of the total number of protons, resulting in $\tilde{\lambda_p}$, and neutrons, resulting in $\tilde{\lambda_n}$:

$$N_p = 2\int_{\infty}^{\tilde{\lambda}} \tilde{g}(\epsilon) d\epsilon. \tag{28}$$

One uses recurrence relations for the Hermite functions:

$$H_{2k}(x) = (-1)^{2k} e^{x^2} \frac{d^{2k}}{dx^{2k}} e^{-x^2} \tag{29}$$

and, hence, solving the integral one obtains

$$N_p = \sum_{i=1}^{\infty}\left[1 + \mathrm{erf}(x_{iF}) - \frac{2}{\sqrt{\pi}} e^{-x_{iF}^2} \sum_{k=1}^{m} a_{2k} H_{2k-1}(x_{iF})\right] \tag{30}$$

where

$$x_{iF} = (\tilde{\lambda} - \epsilon_i)/\gamma, \quad a_{2k} = (-1)^k/(2^{2k}k!). \tag{31}$$

The binary character is included by $\{\epsilon_i\}$, which are the DTCSM single particle energy levels. The final smoothed distribution total energy $\tilde{U}$ is calculated, considering a continuous energy value along the energy range up to the smoothed Fermi level:

$$\tilde{U}_{p,n} = 2\int_{-\infty}^{\tilde{\lambda}_{p,n}} \tilde{g}_{p,n}(\epsilon)\epsilon d\epsilon. \tag{32}$$

The results for proton and neutron level schemes are added for every deformation point. Finally the evolution of the total shell corrections, by summing the proton and neutron terms, is obtained for a given fission channel. After solving the Hermite function dependent integral, the result for the smoothed energy is

$$\tilde{U}_{p,n} = \sum_i \left\{\epsilon_i\left[1 + \mathrm{erf}(x_{iF}) + \frac{1}{\sqrt{\pi}} e^{-x_{iF}^2} \sum a_{2k} H_{2k-1}(x_{iF})\right] + \frac{\gamma}{\sqrt{\pi}} e^{-x_{iF}^2}\left[1 + \sum_{k=1}^{m} a_{2k}(H_{2k} + 4kH_{2k-2})\right\}. \tag{33}$$

One performs the sum up to $m = 3$ for the plateau condition. Then one applies Eq. (24) for protons and neutrons, and sums

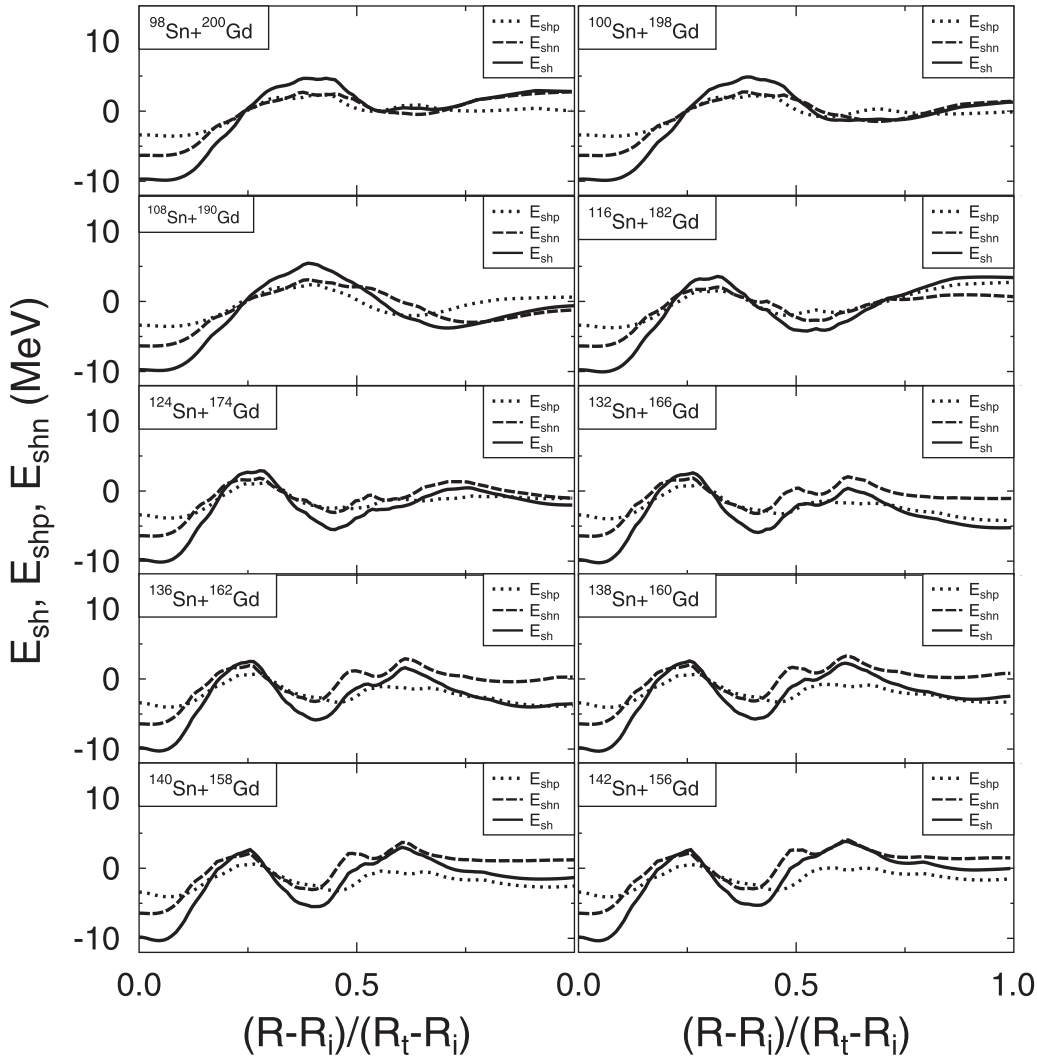

FIG. 4. Proton E_{shell_p}, neutron E_{shell_n}, and total shell correction E_{shell} evolution along the Sn-channel fission paths. One observes the transition from one hump (neutron-poor Sn) towards two-humped behavior (neutron-rich Sn).

the results to obtain the total shell correction for every step of the fission process, along the distance between centers R.

III. RESULTS AND DISCUSSION

Calculations have been performed for the decay of the superheavy nucleus ^{298}Fl. This nucleus is preferred as being considered doubly magic, and hence one of the most stable in the superheavy region. Since the 1960′s, calculations have been made for the stability and possible existence of superheavy nuclei. Theoretical predictions show the region around the doubly magic ^{298}114, later becoming flerovium. Calculations have been made first within the macroscopic-microscopic method, with local and nonlocal potentials [32], emphasizing a center of stability for $Z = 114$ and $N = 184$. A prominent ground state has been also observed within the Woods-Saxon potential, for the ground state of ^{298}114, enforcing this nucleus as being spherically stable [33]. The self-consistent calculations support the prediction of the next doubly magic superheavy as ^{298}Fl [34], where it is demonstrated that $Z = 114$ and $N = 184$ are proton and neutron shell closures, within the calculations with Skyrme SkI4. If one adds the experimental results from Dubna [35] and GSI-Darmstadt [36], one can conclude that ^{298}Fl is considered, if not the most, one of the very stable nuclear systems in the superheavy region. For this reason, calculation of the fission barriers along some specific channels will provide a picture about how this nuclear ground state is capable of survival.

Due to the fact that strong negative shell corrections occur around magicity, two fission channel directions have been chosen for the emitted fragment: Sn and Pb as main reaction partners. One takes advantage of their proton magicity and browses their mass range in order to study which neutron number division is favored for fission.

A. The Sn fission valley

The quasisymmetric isotopic channel of Sn + Gd is studied by varying the neutron division between the two partners.

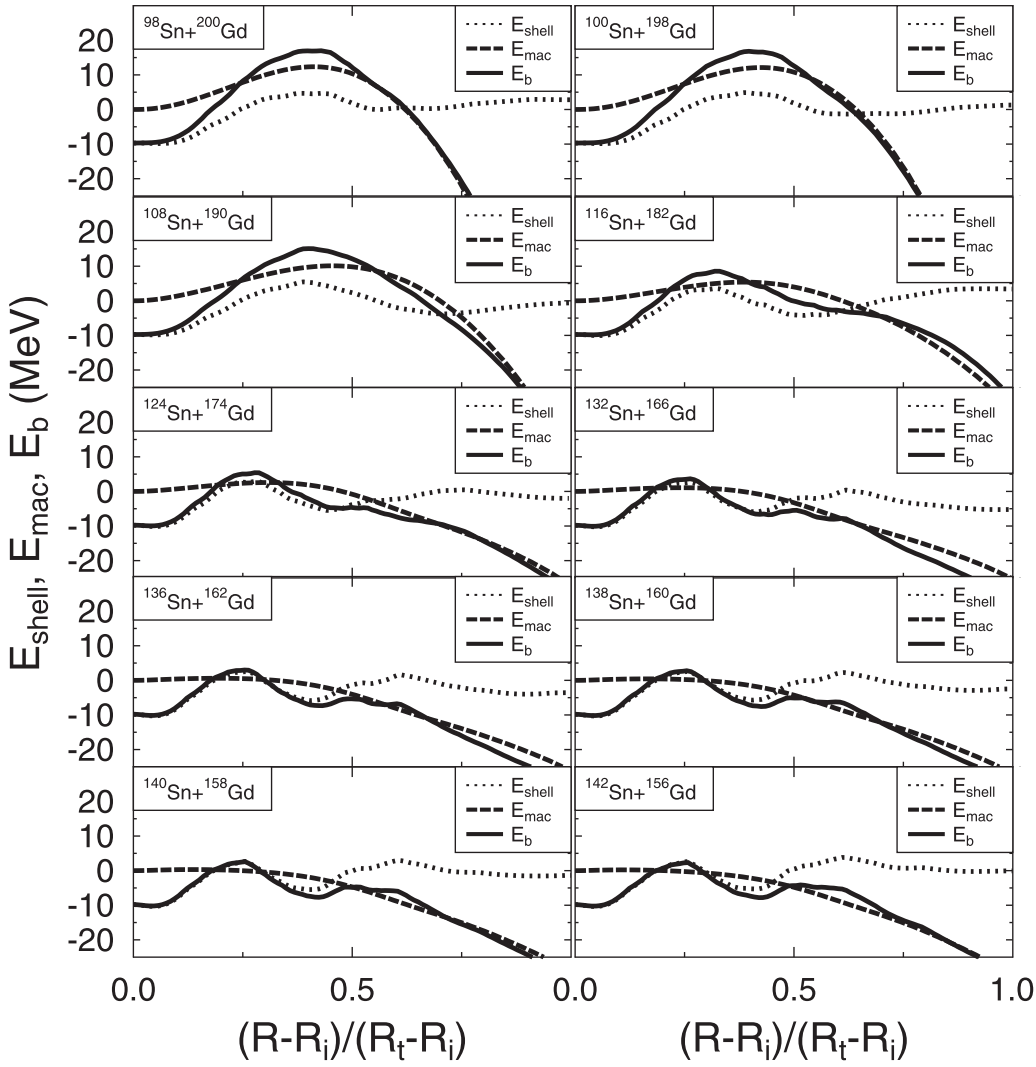

FIG. 5. Shell correction, macroscopic and potential barrier evolution against the reduced distance between centers. One observes the two-humped barriers for more symmetrical reactions ($^{132-142}$Sn fragment).

The browsing covered the doubly magic ^{100}Sn and ^{132}Sn and beyond, up to equal number of neutrons for Sn and Gd. The large part of the barrier is the Yukawa-plus-exponential energy. Even if small, it scales the total deformation energy on account of the shell corrections to play the main role.

As presented, the deformation dependent macroscopic part consists of the Coulomb and the nuclear surface Yukawa-plus-exponential energies. A larger YE energy against the Coulomb part increases the height of the macroscopic barrier. This is the case of the neutron-poor ^{98}Sn fragment, with a 12.35-MeV macroscopic barrier height. As the Sn-neutron number increases, the YE energy decreases. The Coulomb term, though the Z splitting is the same, has a slight variation, thus the macroscopic barrier decreases as the neutron division becomes more symmetrical. This is due to the modifying geometry configuration, since some of the partners are β_2 deformed. Also, since the reactions are considered adiabatic, the charge density varies with the neutron-number variation. A comparison between the composing terms of the macroscopic barrier for the Sn valley is displayed in Fig. 1. One can see that ^{98}Sn has the highest variation curve for the YE term (upper plot), but also the largest (in absolute value) values in Coulomb energy (middle plot). However, the YE surpasses the electrostatic change in this case. The lowest variation curve of the YE energy belongs to ^{142}Sn, making the total macroscopic barrier (lower plot) almost nonexistent. As a partial conclusion, the system prefers neutron symmetry up to now.

The shell effects for the Sn valley are studied next. As discussed above, the first step is to find the Fermi level for protons $\tilde{\lambda}_p$ and neutrons $\tilde{\lambda}_n$, assuming a smoothed level distribution. One solves Eq. (28) for every step along R, the distance between the centers of the fragments, during fission splitting. As the smoothed Fermi level is higher, more levels are accounted for in the averaged energy. R_i is the initial distance between centers, when the emitted fragment is still embedded in the parent, and R_t is the touching point distance. One can observe an increasing tendency for both quantities, slightly more pronounced towards the neutron-rich Sn

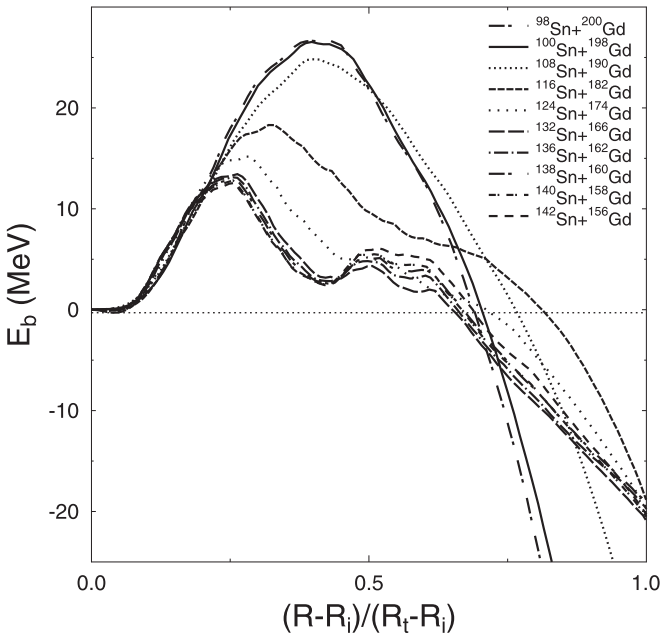

FIG. 6. Fission barriers for Sn-channel reactions from ^{298}Fl. The one-hump behavior for the highest barriers occurs for the neutron-poor Sn reaction, and two-hump barrier shapes take place for the neutron-rich Sn channels.

fragment. This behavior is even more obvious in Fig. 2 where $\tilde{\lambda}_p$ and $\tilde{\lambda}_n$ are shown separately. The neutron-rich ^{138,140,142}Sn have the highest increase towards the final steps of the splitting, for the proton and neutron smoothed Fermi level.

Once the counting limit $\tilde{\lambda}_p$ and $\tilde{\lambda}_n$ is established along every step of the elongation, one calculates the level density $\tilde{g}(\tilde{\lambda})$ for the smoothed level distribution, with Eq. (26). Due to the smoothing function expression in Eq. (27), which contains the exponential, only the levels around $\tilde{\lambda}_p$ and $\tilde{\lambda}_n$ will count. A larger value of $\tilde{g}(\tilde{\lambda})$ will ensure a higher value of the smoothed distribution energy $\tilde{U}$, hence the possibility to have a total negative value of the shell corrections. Negative shell corrections lower the total deformation energy, and consequently one will have a lower fission channel barrier.

TABLE I. YE maximum $E_{\rm mac}^{(\rm max)}$, fission barrier height E_b, and their position on the reduced distance R_n between centers for Sn-channel reactions.

Reaction	$E_{\rm mac}^{(\rm max)}$(MeV)	E_b (MeV)	R_n
^{98}Sn + ^{200}Gd	12.35	24.94	0.35
^{100}Sn + ^{198}Gd	12.12	26.54	0.39
^{108}Sn + ^{190}Gd	10.11	24.82	0.4
^{116}Sn + ^{182}Gd	5.39	18.3	0.32
^{124}Sn + ^{174}Gd	2.57	14.93	0.27
^{132}Sn + ^{166}Gd	1.07	13.44	0.26
^{136}Sn + ^{162}Gd	0.60	13.13	0.25
^{138}Sn + ^{160}Gd	0.31	12.96	0.25
^{140}Sn + ^{158}Gd	0.31	12.81	0.25
^{142}Sn + ^{156}Gd	0.23	12.57	0.26

TABLE II. YE maximum $E_{\rm mac}^{(\rm max)}$, fission barrier height E_b, and their position on the reduced distance between R_n centers for Pb-channel reactions.

Reaction	$E_{\rm mac}^{(\rm max)}$(MeV)	E_b (MeV)	R_n
^{182}Pb + ^{116}Ge	0.13	8.44	0.28
^{186}Pb + ^{112}Ge	0.32	9.29	0.29
^{190}Pb + ^{108}Ge	0.86	10.54	0.30
^{194}Pb + ^{104}Ge	2.07	12.61	0.27
^{198}Pb + ^{100}Ge	2.57	14.93	0.28
^{202}Pb + ^{96}Ge	2.96	15.46	0.30
^{208}Pb + ^{90}Ge	2.97	17.33	0.46
^{212}Pb + ^{86}Ge	4.06	19.82	0.50
^{216}Pb + ^{82}Ge	7.54	22.59	0.58
^{220}Pb + ^{78}Ge	9.15	26.71	0.55
^{224}Pb + ^{74}Ge	8.62	23.92	0.53
^{228}Pb + ^{70}Ge	10.97	25.86	0.54
^{232}Pb + ^{66}Ge	12.53	29.53	0.49
^{236}Pb + ^{62}Ge	15.12	31.45	0.51
^{240}Pb + ^{58}Ge	18.58	33.46	0.53

For the evolution of the proton and neutron smoothed level density distributions, $\tilde{g}_p(\tilde{\lambda}_p)$ and $\tilde{g}_n(\tilde{\lambda}_n)$, at the smoothed Fermi levels, with the reduced elongation, a generally decreasing behavior is observed, due to the decreasing level density, both for protons and neutrons, as the nuclear mass decreases. This is the effect of the increase of the distance between levels for lighter nuclei (the $\sim A^{-1/3}$ dependence). The neutron level density is seen to be rapidly decreasing since one increases the neutron number for the Sn partner, in the second part of the splitting region. However, the higher $\tilde{g}_p(\tilde{\lambda}_p)$ values along the first region ensure a higher range of smoothed distribution energy, and thus a higher value for $\tilde{U}$. One point to be observed is that the doubly magic ^{132}Sn does not account for the highest smoothed proton level densities along the overlapping region.

A comparison between the smoothed density functions is presented in Fig. 3, for protons $\tilde{g}_p(\tilde{\lambda}_p)$ (upper plot) and for neutrons $\tilde{g}_n(\tilde{\lambda}_n)$. Since the proton partition does not change, the variations for $\tilde{g}_p(\tilde{\lambda}_p)$ are entirely due to the geometrical differences along the splitting. The final region of elongation produces the largest shape changes, ending at the two final fragment deformations, and hence the strongest level density variation. Due to the neutron partition variation, the neutron smoothed density $\tilde{g}_n(\tilde{\lambda}_n)$ varies sooner with elongation against different Sn and Gd isotopes. Each of the two distribution densities produces the final smoothed energy $\tilde{U}_p$ (protons) and $\tilde{U}_n$ (neutrons), which are subtracted from the corresponding sum of the real DTCSM energy levels, resulting in the proton and neutron shell corrections by Eq. (24).

The proton, neutron, and total shell corrections are displayed in Fig. 4 for all the Sn + Gd fragment pairs. One can see a prominent minimum at the beginning of the splitting process for all pairs. This minimum is responsible for the pocket in the total potential, allowing a quasistable position for the ground state of ^{298}Fl. A one-hump behavior can be observed for neutron-poor Sn reactions. As the neutron number $N_{\rm Sn}$ increases, a second minimum appears both in proton

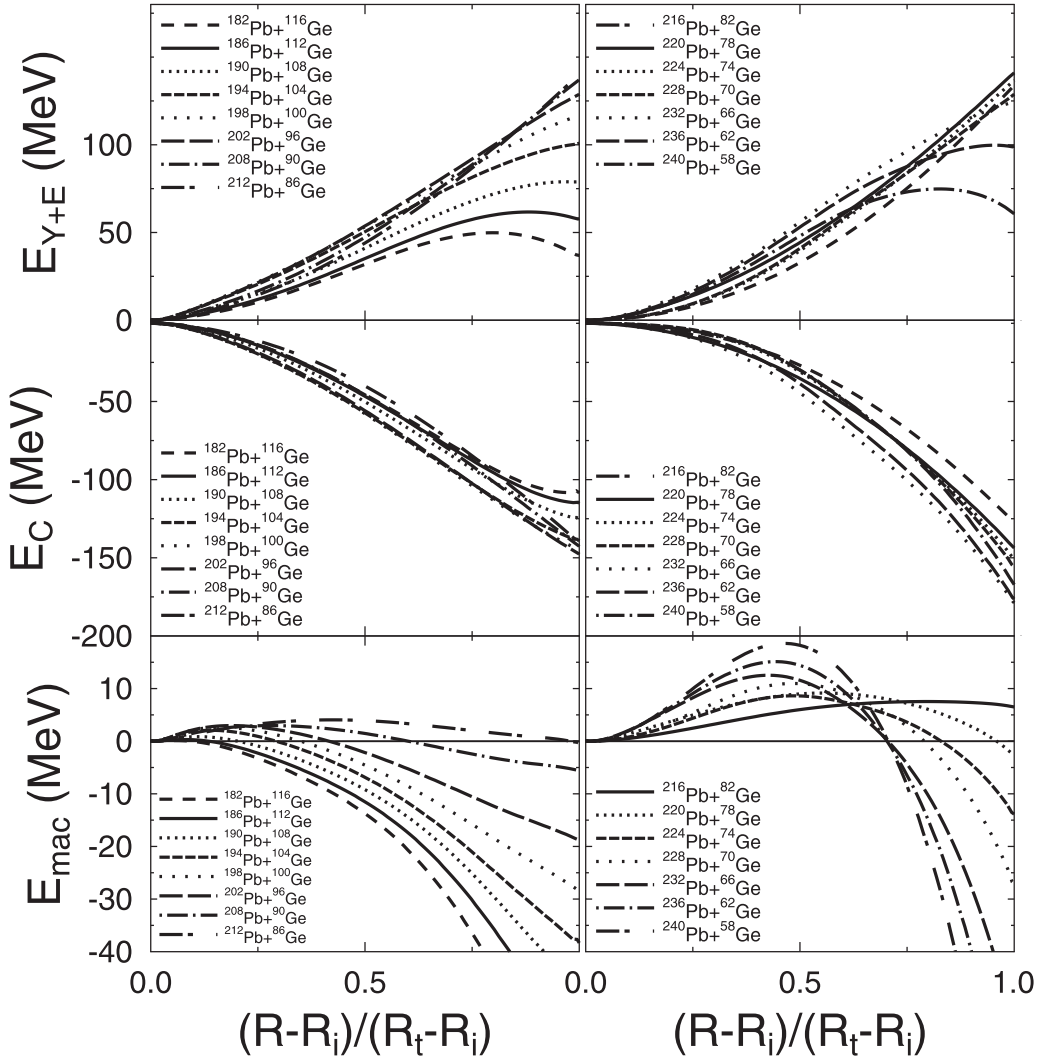

FIG. 7. Comparison between the macroscopic components of the fission barrier for the Pb fragment: the Yukawa-plus-exponential energies (upper plot), the Coulomb term (middle plot), and the total charged liquid drop energies as a function of reduced elongation. The YE term takes larger values as the Pb-neutron number increases, and consequently the macroscopic barrier is lower for neutron-poor Pb-partner reactions (^{182}Pb is the lowest).

and neutron, and subsequently in the total shell correction energy. This kind of behavior will generate the well-known double-humped fission barriers. The Sn-valley fission barriers thus obtained, as the sum of macroscopic and shell correction energies, are displayed in Fig. 5, together with their components. The one-hump barrier is visible for the neutron-poor Sn fragment reaction, as generated by the shell correction evolution. As the Sn mass number increases, the barrier starts to display the second hump, induced also by shell effects. The important feature one can observe is the drastic decrease in height and width of the barrier, once the fragment masses are closer to each other. This trend is also due to the macroscopic part of the deformation energy: the system lowers the liquid drop term, via the Yukawa-plus-exponential part, and the Coulomb energy increases. The result is a lowering of the total fission barrier as the system becomes more symmetric.

The comparison between the Sn-reaction fission barriers is presented in Fig. 6. The barriers have been scaled to the ground state energy of ^{298}Fl. The height is maximum for the largest mass asymmetry, with ^{98}Sn. It nearly constantly decreases as the neutrons are quasisymmetrically disposed. At the same time, the double-humped appearance becomes more visible. Another aspect worth mentioning is the exit point from the barrier. The reduced distance between fragment centers, $(R - R_i)/(R_t - R_i)$, is 1 at the touching point (tangent configuration). All reactions are out of the barrier way before that point, meaning the exit point takes place when the fragments are still partially overlapped. Table I presents the height of the Sn-valley fission reaction, together with the reduced distance point where the maximum occurs. One can see the difference of more than half height ($\approx$ 14 MeV) between the highest (^{100}Sn) and lowest (^{142}Sn) barrier. An interesting observation would be that the double magicity of ^{100}Sn and the even stronger ^{132}Sn does not ensure a much lower fission barrier. The reaction channel is influenced also by the macroscopic part and the other partner (Gd) shell corrections.

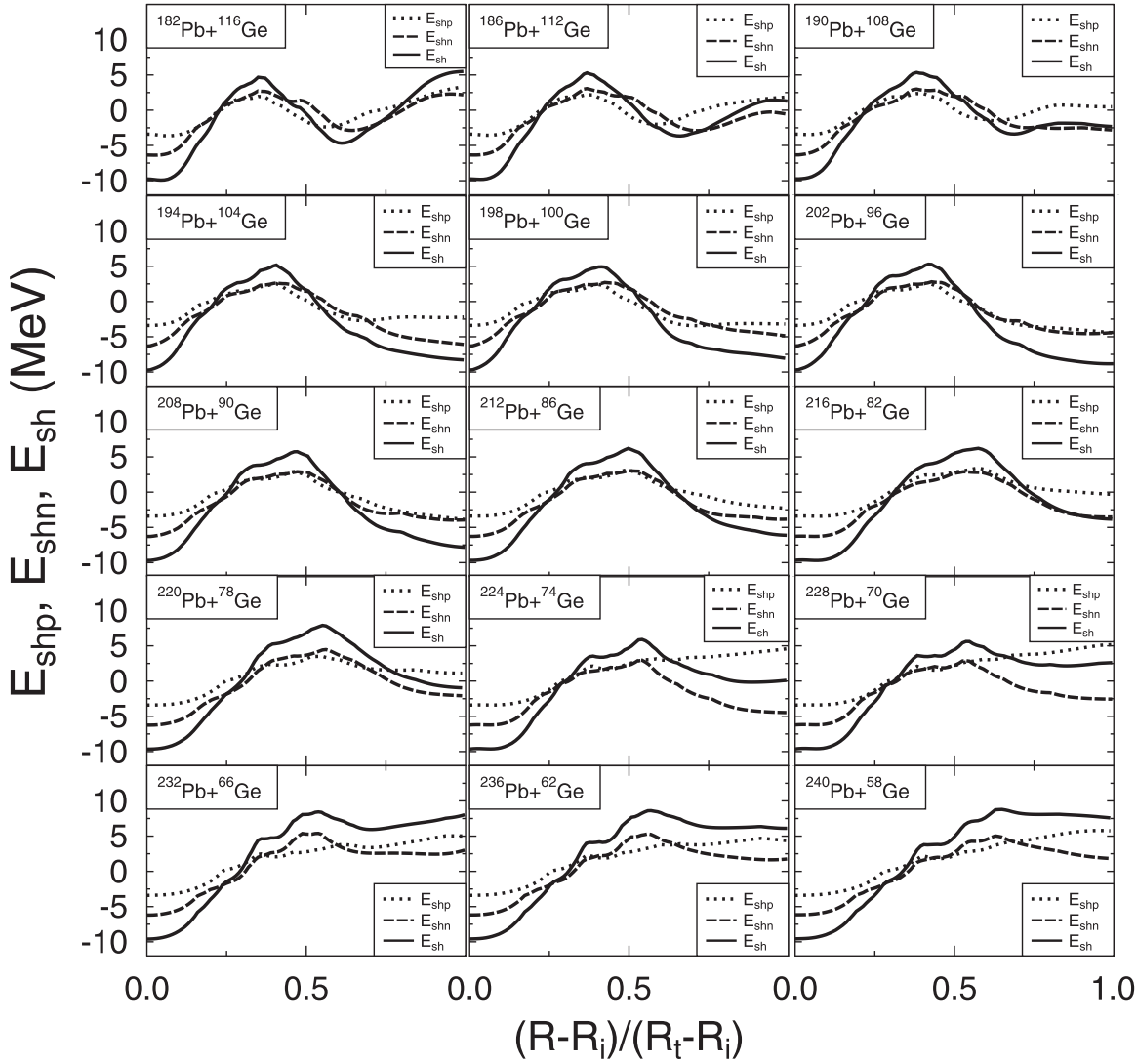

FIG. 8. Proton E_{shell_p}, neutron E_{shell_n}, and total shell correction E_{shell} evolution along the Pb-channel fission paths. One observes the transition from two-hump (neutron-poor Pb) towards one-humped shell correction (neutron-rich Pb), the reverse behavior against the Sn case.

There is no influence from the shell closure during the overlapping region.

B. The Pb fission valley

The study of the Pb valley follows the same chain of steps as the Sn one. One starts from the very neutron-poor ^{182}Pb up to the neutron-rich ^{240}Pb accompanied fission.

The macroscopic behavior is completely reversed against the Sn channel cases. A weak YE energy results in the lowest macroscopic barrier for the ^{182}Pb reaction. As the neutron number increases for Pb isotopes, the YE nuclear surface term increases also. Slow variations are observed for the Coulomb term, due mainly to different deformation paths. In Fig. 7, the macroscopic terms are compared, together with the total macroscopic part. The smallest difference is observable when neutron-poor Pb fragments are present. As the Pb neutron number increases, so does the macroscopic barrier. Contrary to the Sn case, the highest charged liquid drop energy is attained for neutron-rich Pb fragment reactions. If the $^{182-190}$Pb channels have practically no macroscopic barriers (0.13–0.9 MeV), the ^{240}Pb reach a 19-MeV height. Again, the tendency towards mass symmetry is dominant for the macroscopic part.

One adds the shell correction energy now. Once the energy levels are obtained within the deformed two-center shell model, they are input data for the microscopic part of the deformation energy. The calculations are made separately for protons and neutrons, and the results are summed.

Figure 8 presents the shell correction variation with the reduced distance between centers for all the Pb channels that have been considered. Though not the same, the variation curves for proton and neutron shell corrections follow more or less the same trend. A first minimum is present for all reactions. This minimum will generate the ground state for ^{298}Fl, similar to the Sn cases. Then a second minimum

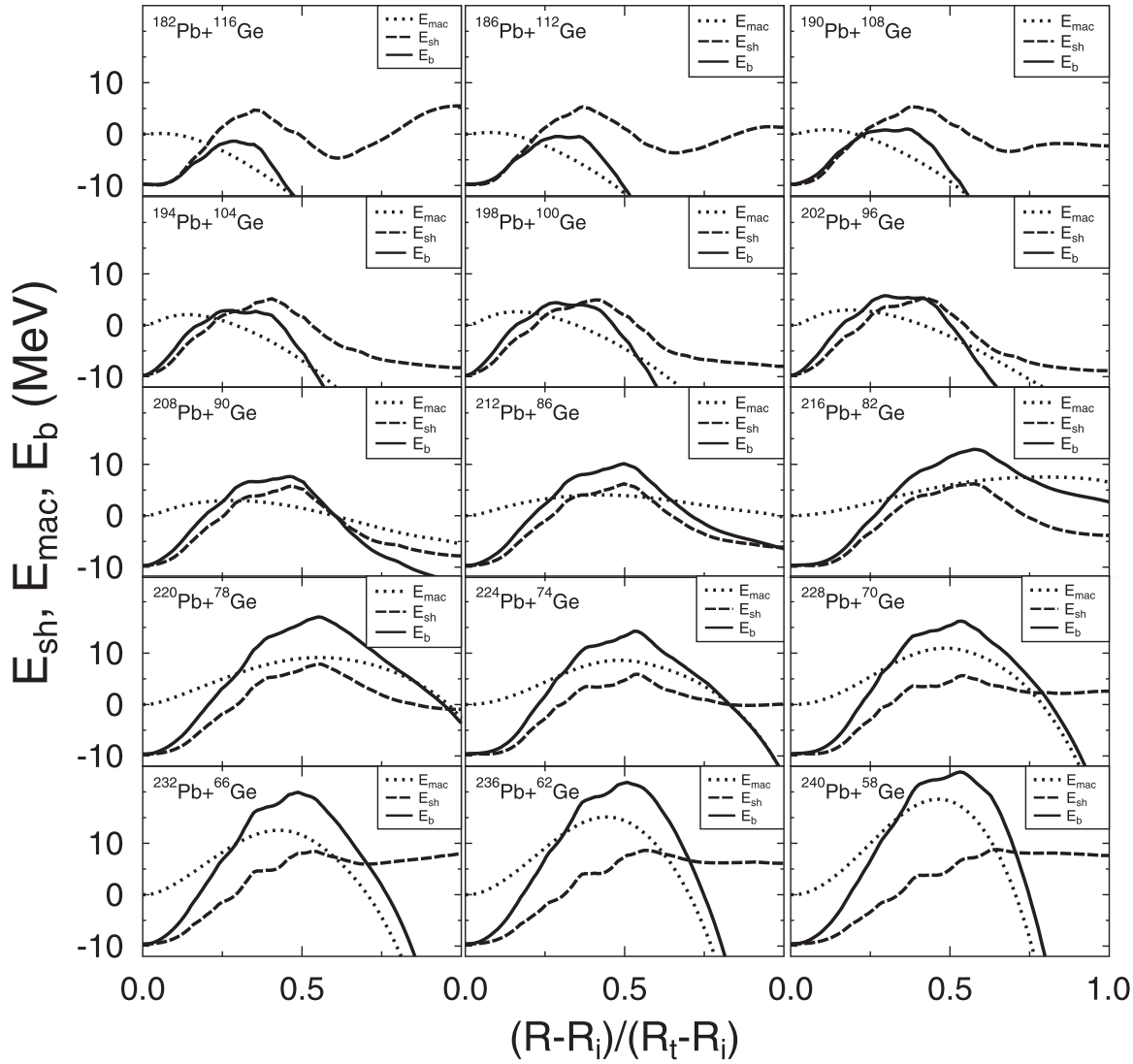

FIG. 9. The YE charged liquid drop $E_{\rm mac}$, shell correction $E_{\rm shell}$, and total barrier E_b against the reduced distance between fragment centers, for Pb fission channels from ^{298}Fl. The macroscopic term heightens as the Pb neutron number increases. The shell corrections dictates the shape of the barrier.

appears for neutron-poor Pb fragments, that will induce the double-humped final fission barrier for that specific reaction channel. The second minimum gradually disappears, as the Pb neutron number increases. An observable feature is that the shell correction values do not vary too much in height from one channel to another, but the shape of the curves does. As a particular feature, one can see the low minimum of the total corrections at the end of the splitting for ^{208}Pb. Obviously, this is due to the strong double magicity ($Z = 82, N = 126$) of the heavy fragment. Another final prominent minimum is visible for ^{216}Pb + ^{82}Ge, because of the magic $N = 50$ of Ge, besides the Pb proton number. The macroscopic YE and the shell corrections are added and the final fission barrier for a certain reaction channel is obtained.

A comparative result is displayed in Fig. 9. The abrupt decrease in macroscopic YE energy cuts off the shell corrections for neutron-poor $^{182-194}$Pb, which have a much lower barrier height than the neutron-richer Pb isotopes reactions. One can see that the second part of shell corrections has no role for these reactions. Once the Pb mass number increases, so does the barrier height. Also, the width of the fission barrier increases drastically, even though, for example, ^{208}Pb should have been advantaged by its double magicity at the end of the decay process.

A comparison between the Pb barriers, scaled to the ground state energy, is presented in Fig. 10 as a function of the reduced distance between centers. The first range of these deformation energies, $^{182-212}$Pb (left plot), shows a height domain between 8.44 MeV (^{182}Pb) and 19.82 MeV (^{212}Pb). The lowest height is also connected with the smallest width: the exit point from the barrier lies down at less than half the distance between centers. The second range of the reactions, $^{216-240}$Pb, has a height domain between 22.6 MeV (^{216}Pb) and 33.46 MeV (^{240}Pb). Hence, the behavior of the total deformation energy is completely opposite to the Sn valley: as the neutron number of Pb increases, the barrier height increases

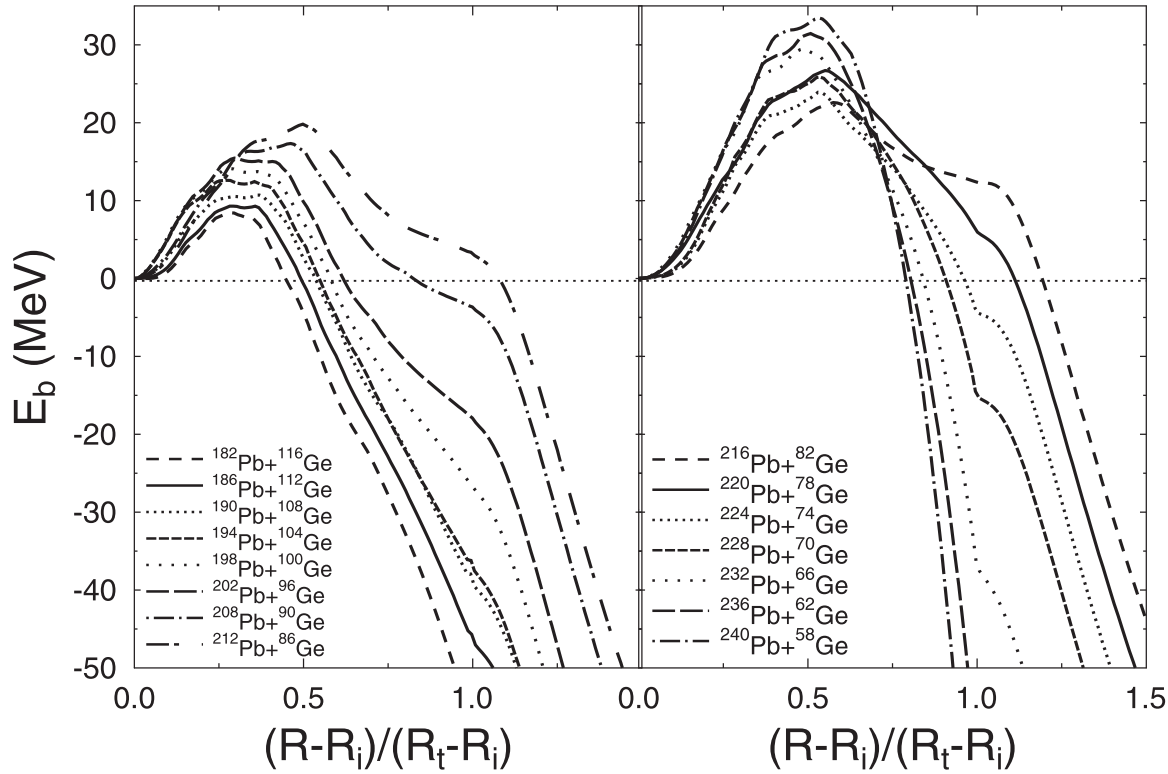

FIG. 10. Fission barriers for Pb-channel reactions from ^{298}Fl. The fission barriers are lower and narrower as the system tends towards mass symmetry, hence for the neutron-poor Pb reaction partner.

as well, and the width becomes larger. The barrier values are presented in Table II. The explanation comes out from the two deformation energy terms: the system tends to mass symmetry beyond charge symmetry. This tendency is mainly due to the Yukawa short range forces in the macroscopic part and the deformation dependent shell corrections, via smoothed Fermi levels, in the microscopic one. The shell corrections are not very influential within the partially overlapping region, but magicity manifests itself at the end, upon the second part of the fission barrier. The lowest fission barriers are obtained for neutron-rich Sn accompanied fission $^{138-142}$Sn $\approx$ 12-MeV height, and for the neutron-poor Pb channel, around 8.44 MeV (^{182}Pb), 9.29 MeV (^{186}Pb), and 10.54 MeV (^{190}Pb).

IV. CONCLUSIONS

A highly specialized binary macroscopic-microscopic method has been developed to calculate the fission barriers around two microscopically, via shell effects, advantaged fragments. Sn and Pb fragments have been chosen due to their proton magicity. Neutron magicity has been covered as well. A slight dominance of the Coulomb forces against the nuclear short range Yukawa-plus-exponential ones decreases the fission barrier in the neutron-rich Sn region. Both proton and neutron shell corrections contribute to the lowering of the Sn fission valley barrier when the system inclines towards mass symmetry, via the neutron-rich Sn accompanied reaction.

The reverse is available for the Pb valley. Neutron-poor ^{182}Pb displays the lowest height (8.44 MeV) together with the narrowest width. As the Pb neutron number increases, both the macroscopic part and the shell corrections enlarge the barriers. Double magicity for ^{100,132}Sn or ^{208}Pb plays no role in the overlapping region of the fragments. Their negative shell correction effect manifests only at the end of the splitting, beyond the exit point of the fission barrier.

ACKNOWLEDGMENTS

This work is supported by the Ministry of Research, Romania, through the Nucleu Program 2022, and Frankfurt Institute for Advanced Studies, Frankfurt am Main, Germany.

[1] I. Muntian and A. Sobiczewski, Fission barriers of heavy and superheavy nuclei, in *Structure and Dynamics of Elementary Matter*, NATO Science Series Vol. 166, edited by W. Greiner, M. G. Itkis, J. Reinherdt, and M. C. Guclu (Springer, New York, 2004).

[2] S. Hofmann, S. Heinz, and A. V. Yeremin, Remarks on the fission barriers of superheavy nuclei, Eur. Phys. J. A **52**, 116 (2016).

[3] S. Hofmann *et al.*, Fission barriers of super-heavy nuclei and search for element 120, in *Fission and Properties*

of Neutron-Rich Nuclei (World Scientific, Singapore, 2017), p. 88.
[4] J. R. Nix, Calculation for fission barriers for heavy and superheavy nuclei, Annu. Rev. Nucl. Sci. **22**, 65 (1972).
[5] G. Royer, M. Prince, X. Scannell, I. Lele-Cheudjou, and A. Samb, Fusion reactions and synthesis of some superheavy nuclei, Nucl. Phys. A **1000**, 121811 (2020).
[6] M. Kowal, T. Cap, P. Jachimowicz, J. Skalski, K. Siwek-Wilczyńska, and J. Wilczyński, Fusion-fission probabilities, cross sections, and structure notes of superheavy nuclei, EPJ Web Conf. **131**, 04005 (2016).
[7] G. Henning, T. L. Khoo, A. Lopez-Martens, D. Seweryniak, M. Alcorta, M. Asai, B. B. Back, P. F. Bertone, D. Boilley, M. P. Carpenter, C. J. Chiara, P. Chowdhury, B. Gall, P. T. Greenlees, G. Gurdal, K. Hauschild, A. Heinz, C. R. Hoffman, R. V. F. Janssens, and A. V. Karpov, Fission Barrier of Superheavy Nuclei and Persistance of Shell Effects at High Spin: Cases of ^{254}No and ^{220}Th, Phys. Rev. Lett. **113**, 262505 (2014).
[8] X. Bao, G. Royer, H. Zhang, and H. Zhang, Spontaneous fission half-lives of heavy and superheavy nuclei within a generalized liquid drop model, Nucl. Phys. A **906**, 1 (2013).
[9] K. Pomorski, A. Dobrowolski, B. Nerlo-Pomorska, M. Warda, J. Bartel, Z. Xiao, Y. Chen, L. Liu, J-L. Tian, and X. Diao, On the stability of superheavy nuclei, Eur. Phys. J. A **58**, 77 (2022).
[10] Y. Qiang, J. C. Pei, and P. D. Stevenson, Fission dynamics of compound nuclei: Pairing versus fluctuations, Phys. Rev. C **103**, L031304 (2021).
[11] H. Flocard, P. Quentin, D. Vautherin, M. Veneroni, and A. K. Kerman, Self-consistent calculation of the fission barrier of ^{240}Pu, Nucl. Phys. A **231**, 176 (1974).
[12] D. Dalili, J. Nemeth, and C. Ngo, A self-consistent Thomas-Fermi calculation of fission barriers at finite temperature and angular momentum as applied to the ^{205}At, Z. Phys. A **321**, 335 (1985).
[13] M. Warda, J. L. Egido, L. M. Robledo, and K. Pomorski, Self-consistent calculations of fission barriers in Fm region, Phys. Rev. C **66**, 014310 (2002).
[14] T. Bürvenich, M. Bender, J. A. Maruhn, and P.-G. Reinhard, Systematics of fission barriers in superheavy elements, Phys. Rev. C **69**, 014307 (2004).
[15] A. Staczak, J. Dobaczewski, and W. Nazarewicz, Self-consistent study of fission barriers of even-even superheavy nuclei, AIP Conf. Proc. **798**, 93 (2005).
[16] J. C. Pei, W. Nazarewicz, J. A. Sheikh, and A. K. Kerman, Fission Barriers of Compound Superheavy Nuclei, Phys. Rev. Lett. **102**, 192501 (2009).
[17] K. P. Santhosh and V. Safoora, Predictions of probable projectile-target combinations for the synthesis of superheavy isotopes of Ts, Phys. Rev. C **95**, 064611 (2017).
[18] K. P. Santhosh and A. Cyriac, Quaternary fission in $^{244-254}$Cf isotopes with two alpha-paricles as middle fragments, Phys. Rev. C **101**, 044613 (2020).
[19] K. Mahata, S. Kailas, and S. S. Kapoor, Fission barrier, damping of shell correction, and neutron emission in the fission of A ≈200, Phys. Rev. C **92**, 034602 (2015).
[20] S. Kumar, Alpha decay chains study for the recently observed superheavy element Z=117 within the isospin cluster model, Phys. Rev. C **85**, 024320 (2012).
[21] S. Kumar, M. Balasubramaniam, R. K. Gupta, G. Münzenberg, and W. Scheid, The formation and decay of superheavy nuclei produced in ^{48}Ca reactions, J. Phys. G **29**, 625 (2003).
[22] C. Samanta, P. R. Chowdhury, and D. N. Basu, Predictions of alpha decay halflives of heavy and superheavy elements, Nucl. Phys. A **789**, 142 (2007).
[23] P. R. Chodhury, C. Samanta, and D. N. Basu, Alpha-decay halflives of new superheavy elements, Phys. Rev. C **73**, 014612 (2006).
[24] R. K. Gupta, M. Balasubramaniam, R. Kumar, N. Singh, M. Manhas, and W. Greiner, Optimum orientations of deformed nuclei for cold synthesis of superheavy elements and the role of higher multipole deformation, J. Phys. G **31**, 631 (2005).
[25] N. Sharma, A. Kaur, and M. Sharma, Ternary fission analysis of ^{242,258}Fm nuclei using equatorial and collinear ckuster tripartition configurations, Phys. Rev. C **105**, 044602 (2022).
[26] H. J. Krappe, J. R. Nix, and A. J. Sierk, Unified nuclear potential for heavy ion elastic scattering, fusion and ground-state masses and deformations, Phys. Rev. C **20**, 992 (1979).
[27] D. N. Poenaru, M. Ivascu, and D. Mazilu, Folded Yukawa-plus-exponential model for nuclei with different charge densities, Comput. Phys. Commun. **19**, 205 (1980).
[28] E. Merzbacher, in *Quantum Mechanics* (Wiley, New York, 1961).
[29] J. Maruhn and W. Greiner, The asymmetric two-center shell model, Z. Phys. **251**, 431 (1972).
[30] A. Diaz-Torres and W. Scheid, Two-center shell model with Woods-Saxon potentials: Adiabatic and diabatic states in fusion, Nucl. Phys. A **757**, 373 (2005).
[31] R. A. Gherghescu, Deformed two-center shell model, Phys. Rev. C **67**, 014309 (2003).
[32] A. Sobiczewski and Z. Patyk, Do the superheavy nuclei really form an island, Phys. Lett. B **186**, 6 (1987).
[33] R. Smolanczuk, J. Skalski, and A. Sobiczewski, Spontaneous fission half-lives of deformed superheavy nuclei, Phys. Rev. C **52**, 1871 (1995).
[34] M. Bender, K. Rutz, P.-G. Reinhard, J. A. Maruhn, and W. Greiner, Shell structure of superheavy nuclei in self-consistent mean-field models, Phys. Rev. C **60**, 034304 (1999).
[35] Y. Oganessian, Synthesis and properties of heaviest nuclei with Z=114–116 in ^{48}Ca induced reactions, Prog. Theor. Phys. Suppl. **146**, 94 (2002).
[36] P. Armbruster, A region of oblate nuclides centred at Z=114 and of spherical nuclides centred at the magic nucleus, EPJ Web Conf. **17**, 12001 (2001).